Journal of Zhejiang University-SCIENCE C (Computers & Electronics)
ISSN 1869-1951 (Print); ISSN 1869-196X (Online)
www.zju.edu.cn/jzus; www.springerlink.com
E-mail: jzus@zju.edu.cn

Self-sensing active magnetic bearing using real-time duty cycle*

Ming TANG[†1,2], Chang-sheng ZHU[2], Jie YU[2]
([1]State Grid Sichuan Electric Power Research Institute, Chengdu 610072, China)
([2]College of Electrical Engineering, Zhejiang University, Hangzhou 310027, China)
[†]E-mail: tangming_king@163.com

Received Jan. 20, 2013; Revision accepted May 17, 2013; Crosschecked July 12, 2013

Abstract: In a self-sensing active magnetic bearing (AMB) system driven by pulse width modulation (PWM) switching power amplifiers, the rotor position information can be extracted from coil current and voltage signals by a specific signal demodulation process. In this study, to reduce the complexity of hardware, the coil voltage signal was not filtered but measured in the form of a duty cycle by the eCAP port of DSP (TMS320F28335). A mathematical model was established to provide the relationship between rotor position, current ripple, and duty cycle. Theoretical analysis of the amplitude-frequency characteristic of the coil current at the switching frequency was presented using Fourier series, Jacobi-Anger identity, and Bessel function. Experimental results showed that the time-varying duty cycle causes infinite side frequencies around the switching frequency. The side frequency interval depends on the varying frequency of the duty cycle. Rotor position can be calculated by measuring the duty cycle and demodulating the coil current ripple. With this self-sensing strategy, the rotor system supported by AMBs can steadily rotate at a speed of 3000 r/min.

Key words: Self-sensing, Active magnetic bearing (AMB), Frequency spectrum characteristic
doi:10.1631/jzus.C1300023 **Document code:** A **CLC number:** TP23

1 Introduction

Active magnetic bearings (AMBs) are being employed in a variety of industrial rotating machineries for their unique features over conventional bearings. Their contact-free suspension provides no lubrication or mechanical friction. Thus, they potentially have the ability to achieve a higher speed. Self-sensing AMBs offer an opportunity to achieve high reliability and low cost by replacing position sensing devices with a specific form of signal processing, which extracts rotor position information from coil current and voltage signals. Self-sensing AMBs have been carried out for years and many methods have been proposed. Recently, intelligence algorithms (Tang and Zhu, 2010) and novel structures such as three-pole AMBs (Garcia *et al.*, 2010) have been studied.

Generally speaking, there are two broad categories of self-sensing AMBs: state observation and modulation. The state observation approach was first proposed by Vischer (1988). His work showed that the AMB state model is controllable and observable with coil current and voltage measured. Rotor position is treated as one of the state variables, which can be reconstructed by a Luenberger observer (Vischer and Bleuler, 1990). However, Vischer's model is very sensitive to the variation of the model parameter. The modulation approach is based on the inductance measurement principle. Similar to an inductance sensor, a high frequency signal with tiny amplitude is injected to the coils of the AMB to measure the variation of coil inductance caused by the rotor displacement. Because of its high frequency (which is much higher than the control signal frequency), the rotor position can be demodulated using a high pass filter (HPF) and other signal process circuits (Sivadasan, 1996). System robustness is then improved

* Project (No. LZ13E070001) supported by the Natural Science Foundation of Zhejiang Province, China

compared to the state observation approach (Montie, 2003). To achieve high efficiency, the pulse width modulation (PWM) switching power amplifiers have been widely used in AMBs (Schammass and Bleuler, 2002). They act not only as actuators, but as an excellent alternative for the high frequency source. In this case, the actuator itself is a position sensor, and thus there is no noncollocation problem, which may introduce difficulty in stabilizing the system. More recent work has focused on how to make good use of this high frequency source (Li *et al.*, 2004; Maslen, 2006; Maslen *et al.*, 2006). However, it remains a challenge to make good use of this excellent alternative because of its intrinsic particularity.

In practical situations, the disturbance force or even electrical noise will inevitably cause current fluctuation. Thus, the duty cycle of PWM is always changing to track the current reference input to generate active magnetic force. It is this time-varying duty cycle that makes PWM different from common high frequency sources.

In general, the high frequency source used for injection has fixed amplitude and frequency, but PWM cannot be simply treated as this kind of conventional high frequency injection. That is, even when the switching frequency of PWM is fixed, its amplitude at the switching frequency cannot be fixed; instead, it varies with the duty cycle. It is the time-varying duty cycle that leads to the complex amplitude-frequency characteristic of PWM. That is where the PWM differs from the conventional sensing signal.

By measuring the frequency component of PWM and current ripple, the equivalent impedance can be calculated by a simple division (Okada *et al.*, 1992; Schammass *et al.*, 2005). To improve the accuracy and bandwidth, Noh (1997) proposed a nonlinear parameter estimator to reject the force feed. More recently, Ranft *et al.* (2011a; 2011b) proposed a coupled reluctance network model by considering the nonlinearity of the magnetic material, to obtain a more accurate estimation of rotor position.

In the above mentioned studies, however, there is no detailed analysis of the frequency spectrum characteristics of coil voltage and current. Furthermore, these methods have a high degree of hardware complexity since both the coil voltage and current are filtered by an analog device. Actually, the coil voltage can be easily measured by the eCAP port of DSP in the form of duty cycle. The demodulation process of coil voltage can also be completed in DSP, to reduce hardware complexity.

In this study we first investigated how the time-varying duty cycle influences the high frequency spectrum characteristics of the coil current and voltage. Mathematical tools including Fourier series, Jacobi-Anger identity, and Bessel function were used to analyze the high frequency component of the coil current. Experimental results confirmed the theoretical analysis. This refined analysis of the current ripple in the frequency domain presents theoretical guidance for the design principle of a band-pass filter (BPF), especially for the selection of the width of the pass band. Then a strategy was proposed using current ripple amplitude and real-time duty cycle to estimate the rotor position. An eight-pole AMB rotor system was used as a platform to evaluate the proposed position estimation scheme. Both static and dynamic experiments were carried out. Using this self-sensing sensor, the AMB rotor system can rotate steadily at a speed of 3000 r/min.

2 Modeling

2.1 Inductor model of AMB

The radial magnetic bearing presented is composed of eight poles (Fig. 1). Two pole pairs are assigned for one degree-of-freedom (DOF).

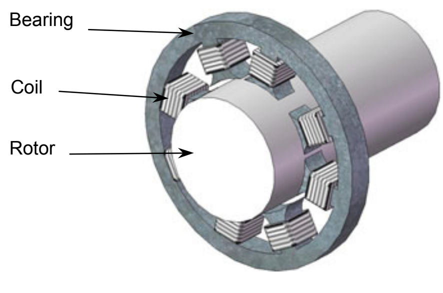

Fig. 1 Radial magnetic bearing structure with eight poles

For simplicity, only one pair of poles is modeled (Fig. 2) to explain the basic principle of the AMBs.

During modeling, some assumptions are made, including edge effect, flux leakage, magnetic saturation, and eddy current losses are neglected; the behavior of the material is linear with constant

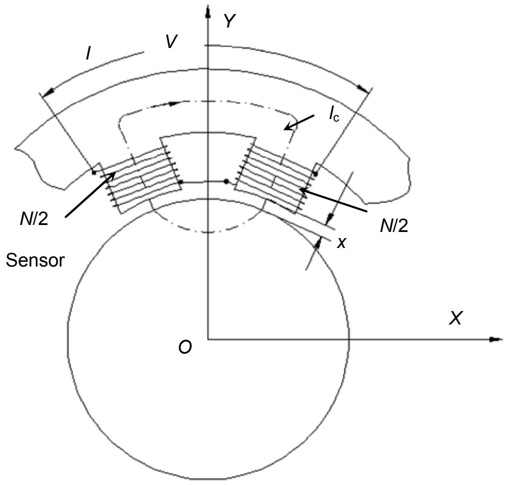

Fig. 2 Electromagnetic loop of the stator and rotor

permeability. Based on the magnetic circuit law, the following equations are obtained:

$$\Phi = \frac{Ni}{R_\mathrm{m}}, \tag{1}$$

$$R_\mathrm{m} = \frac{2x + l_\mathrm{c}/\mu_\mathrm{r}}{\mu_0 A}, \tag{2}$$

$$L = N\frac{\partial \Phi}{\partial i} = \frac{N^2}{R_\mathrm{m}}, \tag{3}$$

where L is the system equivalent inductance, N is the number of coil turns, Φ is the main magnetic flux, i is the coil current, R_m is the total reluctance including the core reluctance and the air gap reluctance, x is the air gap, l_c is the length of the flux path in the core section, μ_r is the relative magnetic permeability, $l_\mathrm{c}/\mu_\mathrm{r}$ stands for the equivalent gap length of the silicon steel sheet, μ_0 is the magnetic permeability of the free space, and A is the cross-sectional area of the flux path at the air gap. Combining Eqs. (2) and (3), L can be obtained as

$$L = \frac{\mu_0 N^2 A}{2x + l_\mathrm{c}/\mu_\mathrm{r}}. \tag{4}$$

According to Kirchhoff's voltage law,

$$V = L\frac{\mathrm{d}i}{\mathrm{d}t} + i\frac{\mathrm{d}L}{\mathrm{d}t} + Ri, \tag{5}$$

where V is the voltage of the coil, and R is the coil resistance. As proved by Noh (1997), the last two terms of Eq. (5) are usually lower than V by an order of magnitude, and can be neglected. Combining Eqs. (4) and (5), the following equation is obtained:

$$\frac{\mathrm{d}i}{\mathrm{d}t} = \frac{2x + l_\mathrm{c}/\mu_\mathrm{r}}{\mu_0 N^2 A}V. \tag{6}$$

It can be concluded from Eqs. (4) and (5) that the system equivalent inductance L and the slope of current di/dt are both functions of the air gap x. Intuitively, air gap x can be obtained by measuring the system equivalent inductance L. This is the basic principle of self-sensing AMBs based on the inductor model.

2.2 Principle of the current mode PWM power amplifier

The current mode PWM power amplifier employed in this work (Fig. 3) has a fixed switching frequency of f_s. It consists of a PD controller, a PWM generator, isolating and driving circuit, half-bridge driving circuit, and a current sensor.

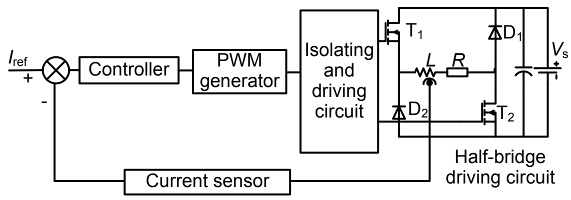

Fig. 3 The general structure of a PWM power amplifier

In general, the current command signal is regarded as a reference signal with low frequency compared to switching frequency, which would be chosen mainly within a range of 10–100 kHz. By changing the duty cycle, this kind of PWM power amplifier can readily trace the current command in a broad frequency bandwidth. A current mode PWM power amplifier can be treated as a low pass filter (LPF) and its bandwidth depends on the bus voltage V_s and the impedance of the load. For pure inductance load, like the coils of AMBs, a phase lag of 90° exists between coil voltage and coil current. Without loss of generality, the current command signal is assumed to consist of the DC and AC components. Though the actual coil current is much more complex, it can be decomposed and analyzed in the form of DC and AC components according to the Fourier decomposition theory. For example, $I_{\text{ref}}(t)$ can be given as

$$I_{\text{ref}}(t) = I_0 + \sum_{n=1}^{\infty} I_n \cos(n\omega_c t), \tag{7}$$

where I_0 is the DC component of the current, and the second term stands for the AC component. I_n is the amplitude of each harmonic component. ω_c is the angular frequency of the current. When only n=1 is considered for simplicity, the duty cycle $\alpha(t)$ can be described as

$$\alpha(t) = \frac{1}{2} + \alpha_m \sin(\omega_c t), \quad 0 \le \alpha_m \le \frac{1}{2}, \tag{8}$$

where α_m is the variation of duty cycle from 50%.

A reference current of 0.5 kHz modulated by this current mode PWM power amplifier with a switching frequency of 20 kHz is shown in Fig. 4, and its frequency spectrum characteristic in Fig. 5.

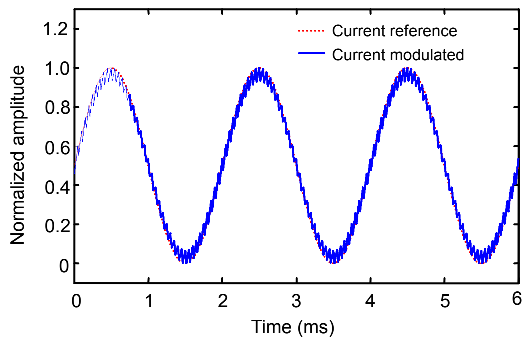

Fig. 4 Demonstration of current modulation

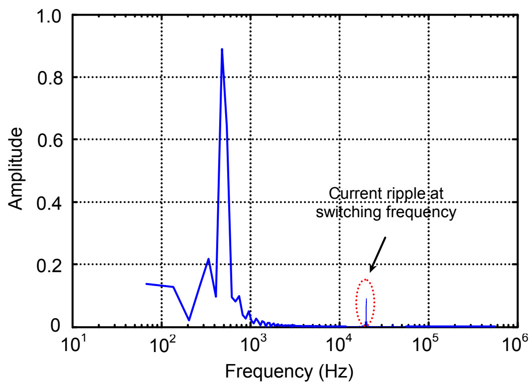

Fig. 5 Frequency spectrum characteristic of modulated current

When analyzing the mechanical dynamic performance of the AMBs, the current ripple is always negligible because of its tiny amplitude. However, this current ripple is the key point for the self-sensing AMBs from which the rotor position can be extracted. Compared to the fundamental frequency caused by mechanical rotor vibrations, the current ripple exhibits a high frequency property. It is the sufficient frequency distance between the fundamental frequency and the current ripple that makes the signal demodulation approach feasible.

3 Frequency spectrum characteristic of coil current

The current ripple is a significant point of the self-sensing AMBs. It is necessary to have a clear knowledge of the frequency component at the switching frequency. First, the coil current is expanded into the form of convergent Fourier series. Then, we make an in-depth analysis of the frequency component at the switching frequency using the Bessel function, to demonstrate the frequency spectrum characteristic of the coil current in detail.

3.1 Analytical expression of coil current at the switching frequency

It is difficult to directly calculate the Fourier series of the coil current, but the Fourier series of the coil voltage can be easily obtained. The Fourier series of the coil current can thus be easily obtained from the Fourier series of the coil voltage. Focusing on a certain period of the switching, and according to Eq. (8), the duty cycle α_k in the kth period can be described as

$$\alpha_k = \alpha(kT_s) = \frac{1}{2} + \alpha_m \sin(\omega_c kT_s), \tag{9}$$

where $T_s=1/f_s$ is the switching period, and the PWM voltage signal of the kth period in the time domain is

$$V(t) = \begin{cases} V_s, & kT_s < t \le kT_s + \alpha_k T_s, \\ -V_s, & kT_s + \alpha_k T_s < t \le (k+1)T_s. \end{cases} \tag{10}$$

V_s is the bus voltage of the power amplifier. The Fourier series of this PWM voltage signal is calculated as follows:

$$\begin{cases} V(t) = a_0 + \sum_{n=1}^{\infty}[a_n \cos(n\omega_s t) + b_n \sin(n\omega_s t)], \\ a_0 = V_s(2\alpha_k - 1),\ a_n = \dfrac{2V_s}{n\pi}\sin(2n\pi\alpha_k), \\ b_n = \dfrac{2V_s}{n\pi}[1-\cos(2n\pi\alpha_k)], \end{cases} \tag{11}$$

or, in another form, as

$$\begin{cases} V(t) = V_s(2\alpha_k - 1) + \sum_{n=1}^{\infty}\dfrac{4V_s}{n\pi}\left|\sin(n\pi\alpha_k)\right|\cos(n\omega_s t + \varphi_n), \\ \varphi_n = \arctan(b_n/a_n) = n\pi\alpha_k, \end{cases} \tag{12}$$

where ω_s is the angular frequency of switching frequency f_s. According to Eq. (12), the current signal $I(t)$ can be described as follows:

$$\begin{cases} I(t) = V_s(2\alpha_k - 1)/(\mathrm{j}\omega_s L) \\ \qquad + \sum_{n=1}^{\infty}\dfrac{4V_s}{\mathrm{j}n\pi\omega_s L}\left|\sin(n\pi\alpha_k)\right|\cos(n\omega_s t + \varphi_n), \\ \varphi_n = \arctan(b_n/a_n) = n\pi\alpha_k. \end{cases} \tag{13}$$

Denote by $i_1(t)$ the frequency component of the coil current at the switching frequency, namely n=1. High-order harmonics are not employed for their tiny amplitudes and low signal-to-noise ratios. According to Eq. (13), $i_1(t)$ can be easily obtained as follows:

$$\begin{cases} i_1(t) = \dfrac{4V_s}{\mathrm{j}\pi\omega_s L}\sin(\pi\alpha_k)\cos(\omega_s t + \varphi_1), \\ \varphi_1 = \arctan(b_1/a_1). \end{cases} \tag{14}$$

By substituting Eq. (4) into Eq. (14), we have

$$\begin{cases} i_1(t) = A_1\cos(\omega_s t + \varphi_1),\ \varphi_1 = \arctan(b_1/a_1), \\ A_1 = \dfrac{4V_s(2x + l_c/\mu_r)}{\mathrm{j}\pi\omega_s\mu_0 N^2 A}\sin(\pi\alpha_k), \end{cases} \tag{15}$$

where A_1 is the amplitude of the current ripple at the switching frequency.

Eq. (15) shows that the amplitude of the current ripple is a function of two variables, air gap x and duty cycle α_k in the time domain. Fig. 6 shows the relationship between A_1, x, and α_k after normalization.

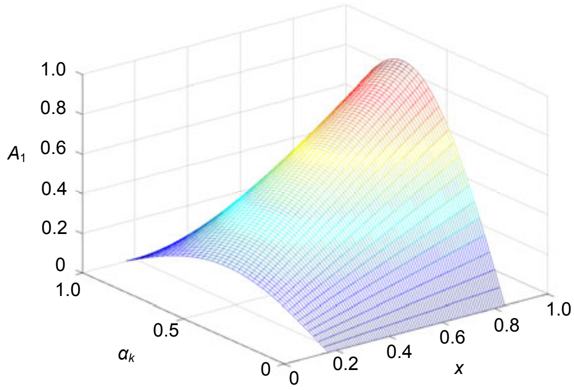

Fig. 6 Relationship between the current ripple, duty cycle, and air gap

Obviously, the air gap x can be easily calculated if A_1 and α_k are measured according to Eq. (15). Real-time duty cycle can be easily obtained by the CAP port of TMS320F28335 (Texas Instruments, USA), and the current ripple amplitude A_1 can also be obtained by a signal demodulation process. However, the BPF in the demodulation process should be carefully designed due to the complex frequency spectrum characteristic of the current ripple. An arbitrary design on the pass band of BPF will reduce the demodulation accuracy of the current ripple and results in inaccurate position estimation.

3.2 Expanded expression of coil frequency spectrum characteristic using the Bessel function

To make an in-depth analysis of the current frequency spectrum characteristic, rewrite Eq. (14) in the following form:

$$i_1(t) = \frac{2V_s}{\mathrm{j}\pi\omega_s L}\{\sin(2\pi\alpha_k)\cos(\omega_s t) + [1-\cos(2\pi\alpha_k)]\sin(\omega_s t)\}. \tag{16}$$

Substituting $\alpha(t)$ in Eq. (8) instead of α_k into Eq. (16), the following equation is obtained:

$$i_1(t) = \frac{2V_s}{\mathrm{j}\pi\omega_s L}\Big[\sin(\omega_s t) - \sin\big(2\pi\alpha_m\sin(\omega_c t)\big)\cos(\omega_s t) + \cos\big(2\pi\alpha_m\sin(\omega_c t)\big)\sin(\omega_s t)\Big]. \tag{17}$$

To expand Eq. (17), the Jacobi-Anger identity is introduced as follows:

$$\exp\left[\frac{x}{2}\left(t-\frac{1}{t}\right)\right]=\sum_{n=-\infty}^{\infty}J_n(x)t^n. \tag{18}$$

Substituting $t=e^{i\phi}$ into Eq. (18), the following equations can be obtained:

$$\sin(2\pi\alpha_m\sin\phi)=2\sum_{n=1}^{\infty}J_{2n-1}(2\pi\alpha_m)\sin[(2n-1)\phi], \tag{19}$$

$$\cos(2\pi\alpha_m\sin\phi)=J_0(2\pi\alpha_m)+2\sum_{n=1}^{\infty}J_{2n}(2\pi\alpha_m)\cos(2n\phi). \tag{20}$$

$J_n(2\pi\alpha_m)$ (n is an integer) is the first kind of Bessel function, and can be described as follows:

$$J_n(2\pi\alpha_m)=\sum_{p=0}^{\infty}\frac{(-1)^p}{p!(p+n)!}\left(\frac{\pi\alpha_m}{2}\right)^{2p+n}. \tag{21}$$

By substituting Eqs. (19) and (20) into Eq. (17), and supposing $\phi=\omega_c t$, the following equation can be obtained:

$$\begin{aligned}i_1(t)=&\frac{2V_s[1+J_0(2\pi\alpha_m)]}{j\pi\omega_s L}\sin(\omega_s t)\\&+\frac{2V_s}{j\pi\omega_s L}J_n(2\pi\alpha_m)\sum_{n=1}^{\infty}\Big[\sin\big(\omega_s t+(-1)^n n\omega_c t\big)\\&+(-1)^n\sin\big(\omega_s t-(-1)^n n\omega_c t\big)\Big],\end{aligned} \tag{22}$$

or, in another form, for a better view of the frequency component:

$$\begin{aligned}i_1(t)=&\frac{2V_s[1+J_0(2\pi\alpha_m)]}{j\pi\omega_s L}\sin(\omega_s t)\\&+\frac{2V_s}{j\pi\omega_s L}\{J_1(2\pi\alpha_m)[\sin(\omega_s t-\omega_c t)-\sin(\omega_s t+\omega_c t)]\\&+J_2(2\pi\alpha_m)[\sin(\omega_s t+2\omega_c t)+\sin(\omega_s t-2\omega_c t)]\\&+J_3(2\pi\alpha_m)[\sin(\omega_s t-3\omega_c t)-\sin(\omega_s t+3\omega_c t)]\\&+J_4(2\pi\alpha_m)[\sin(\omega_s t+4\omega_c t)+\sin(\omega_s t-4\omega_c t)]\\&+\cdots\}.\end{aligned} \tag{23}$$

From the above analysis, it can be concluded that the time-varying duty cycle leads to the rich frequency components in the vicinity of the switching frequency. As displayed by Eq. (23), the frequency components include a center frequency, namely the switching frequency, and infinite side frequencies. The frequency interval between each side frequency is the angular frequency of the reference current ω_c. The amplitude of each side frequency is given by the Bessel function.

4 Experimental results and analysis of current frequency spectrums

The experimental platform, as shown in Fig. 7, includes a rotor and bearing system, an asynchronous induction motor, a current mode power amplifier, a TMS320F28335 control board, and a DL1620 oscilloscope. TMS320F28335 is a 32-bit floating point embedded processor with a calculation speed of up to 150 MIPS. Another advantage of this processor is that it has rich peripherals specially designed for a variety of industrial control, such as ePWM, eCAP, and eCAN. Furthermore, it has 16 channels of 12-bit AD modules on a chip whose accuracy and speed are satisfactory for the control of AMBs. Eight channels of 12-bit DA are extended using DAC7625. AD, DA, and eCAP are the three most important parts used in this self-sensing control strategy. The DL1620 oscilloscope is used to save waveforms and data for post-processing.

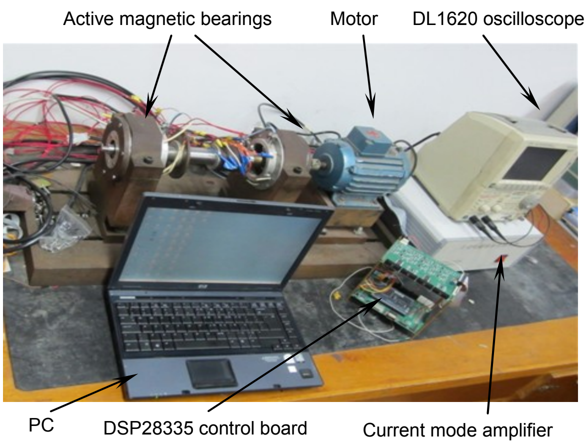

Fig. 7 The experiment platform

Some of the main parameters are V_s=50 V, f_s=20 kHz, N=100. The nominal gap between the rotor and stator is Δr_1=0.35 mm. The nominal gap between the rotor and touchdown bearing is Δr_2=0.25 mm. To minimize the influence of motor and coupling, the left magnetic bearing (away from the motor) in Fig. 7 is chosen to carry out the experiment. According to the mechanical structure, the rotor vertical direction displacement x has a range of 0.1 to 0.6 mm.

This experiment is conducted to test and verify the frequency spectrum characteristic described in Eq. (23). To verify this dualistic function, different x's and ω_c's are tested. However, for the typical AMBs, rotor motion must always be coupled with the current command in the closed feedback loop by the controller. It is impossible to get one without the other in the integral AMB system. Thus, the AMB system is not operated in the normal state, but in a way that suspension is not needed.

With the help of a filler and magnetic force generated by the opposite pole, the rotor can be solidly fixed to make the air gap constant. For example, as shown in Fig. 8, a large current is injected into both lower magnetic poles, in order to generate a magnetic force which is strong enough to hold the rotor down on the touchdown bearing. Different air gaps can be obtained by fillers with different thicknesses stuffed between the rotor and the touchdown bearing.

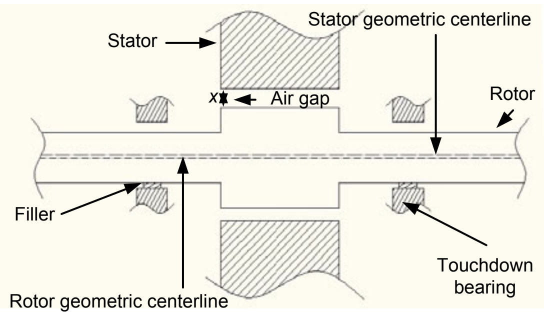

Fig. 8 Schematic of the filler model

As mentioned above, the vertical displacement of the rotor has a range of 0.1 to 0.6 mm. In this experiment, this air gap is divided into six equal parts using fillers each with a thickness of 0.1 mm.

Fig. 9 demonstrates the six different positions of the rotor in the AMB system. Table 1 shows the air gaps and inductances measured in the six positions.

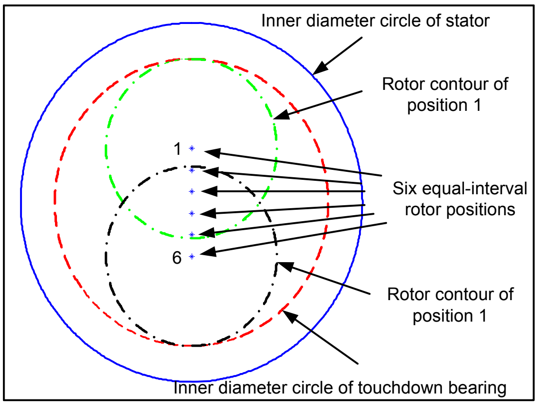

Fig. 9 Six equal-interval rotor positions

Table 1 Inductance of the upper coil at each rotor position

Position	x (mm)	L (mH)
1	0.1	6.01
2	0.2	5.57
3	0.3	5.20
4	0.4	4.88
5	0.5	4.58
6	0.6	4.33

For each rotor position, different frequencies of the reference current are injected into the upper coil. In this experiment, four different f_c are chosen as 0.5, 1.0, 1.5, and 2.0 kHz. On the one hand, when f_c is smaller than 0.5 kHz, the side frequency component will be too close to the center frequency and hard to recognize. On the other hand, the current mode amplifier itself is an LPF with the cut-off frequency of nearly 1 kHz, meaning that higher frequency of the reference current signal will be attenuated. Thus, f_c is chosen between 0.5 and 2.0 kHz. The frequency spectrum of the current ripple at position 1 with different f_c's is shown in Fig. 10. The experimental results agree with the theoretical analysis. The peaks not only occur at the right frequencies, but also have the right amplitudes. The amplitude of the center frequency decreases as the frequency of the reference current increases. The frequency interval between each side frequency component is equal to the frequency of the reference current f_c.

However, the experimental results and theoretical values are not exactly the same at some peaks. This is caused probably by some unavoidable effects such as measurement, input and output noise, and

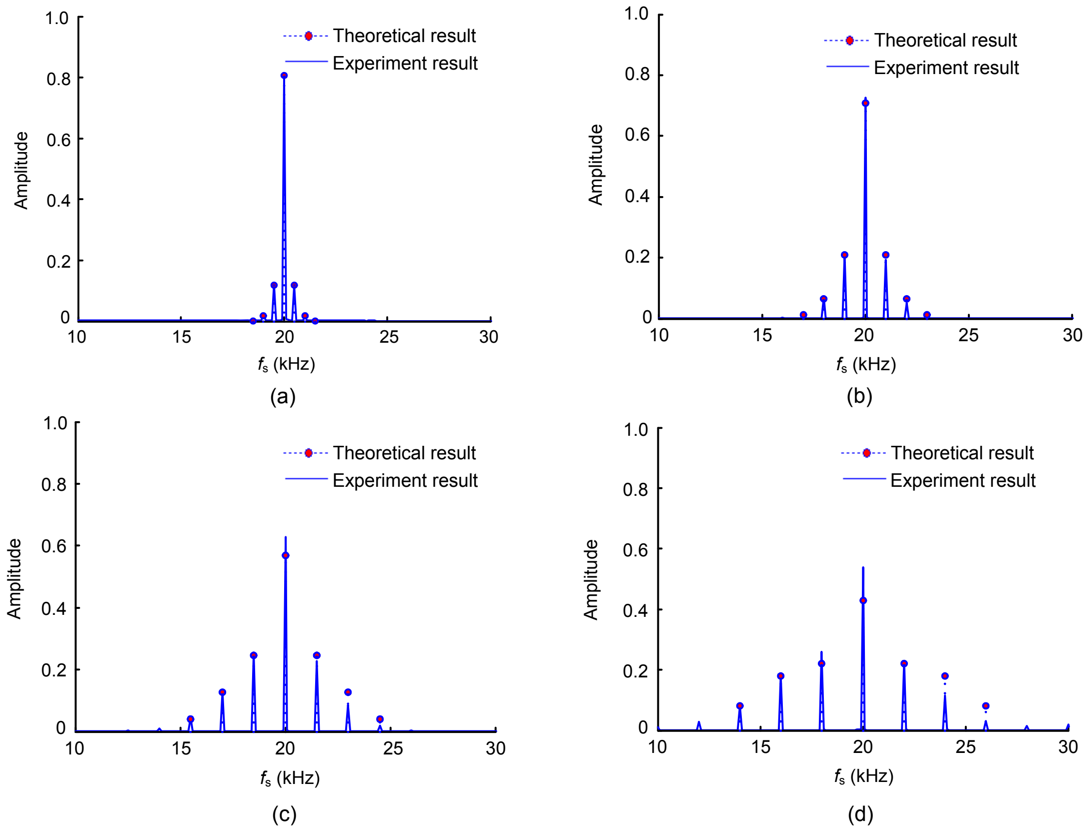

Fig. 10 Frequency spectrum of the current ripple for different f_s's at position 1 (x=0.1 mm)
(a) f_c=0.5 kHz; (b) f_c=1.0 kHz; (c) f_c=1.5 kHz; (d) f_c=2.0 kHz

even some unexpected electromagnetic interference and other nonlinear factors.

The comparisons between theoretical values and experimental results of other positions are shown in Fig. 11.

5 Self-sensing scheme using real-time duty cycle

We can rewrite Eq. (15) as

$$x = f(A_1, \alpha_k) = \frac{\mathrm{j}\pi\omega_s\mu_0 N^2 A A_1}{8V_s \sin(\pi\alpha_k)} - \frac{l_c}{2\mu_r}. \quad (24)$$

Eq. (24) presents a clear functional relationship according to which x can be calculated. The one degree of freedom (1-DOF) structure of the position estimation scheme is shown in Fig. 12.

The envelop extractor is composed of a BPF, an absolute function (ABS), and an LPF that is cascaded to realize demodulation and extraction of coil current. The envelop extractor receives the current signal from the amplifier and produces the current ripple amplitude A_1 as its output. PWM signal is attenuated by 0.2 to match the voltage level of the DSP. α_k is obtained through the eCAP port. The estimated position is then calculated and fed back to the controller according to Eq. (24). Other degrees of freedom employ the same scheme.

6 Bandwidth of the BPF

The complicated frequency spectrum of the current ripple makes it a challenge to extract its amplitude without distortion. It is necessary to choose a proper passband width of the BPF. According to the Parseval theorem, the total energy of a signal is identical to the sum of the energy of all its components in the complete orthogonal function set. So, A_1 can be extracted without distortion only if all the side frequencies of A_1 are included in the BPF. However, it

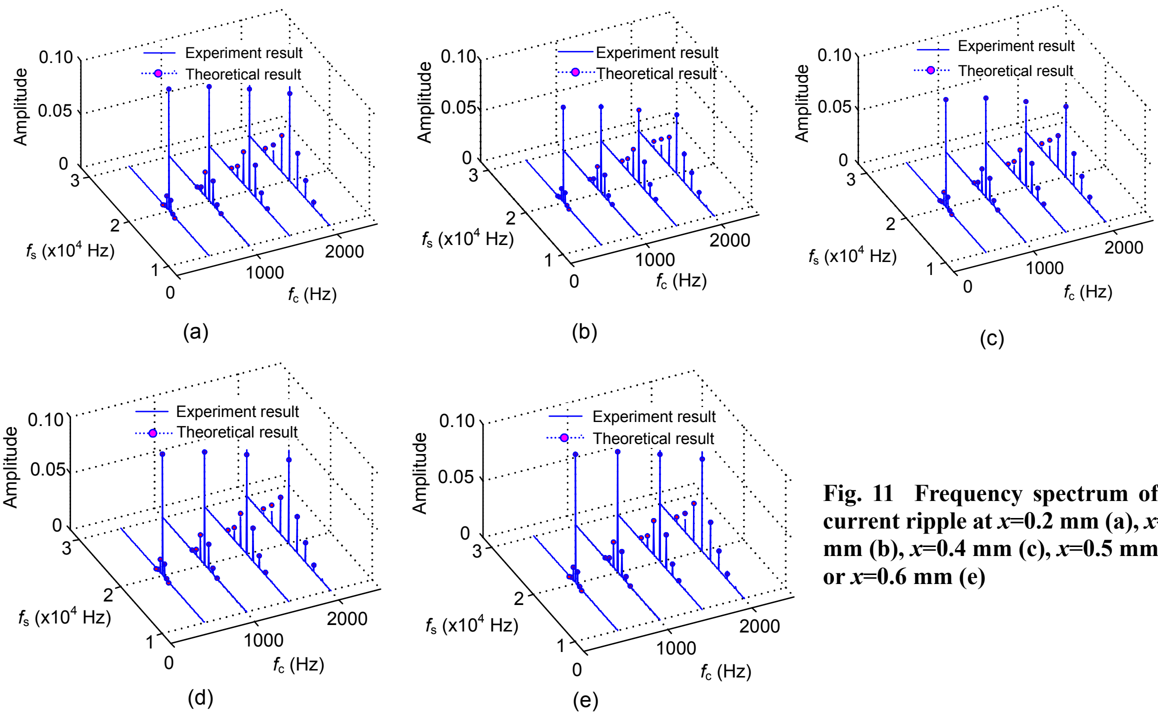

Fig. 11 Frequency spectrum of the current ripple at x=0.2 mm (a), x=0.3 mm (b), x=0.4 mm (c), x=0.5 mm (d), or x=0.6 mm (e)

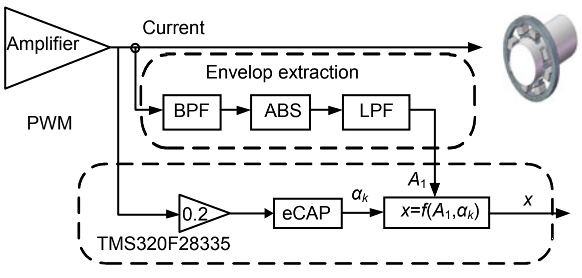

Fig. 12 One degree of freedom (1-DOF) structure of the position estimation scheme

PWM: pulse width modulation; BPF: band-path filter; ABS: absolute function; LPF: low pass filter

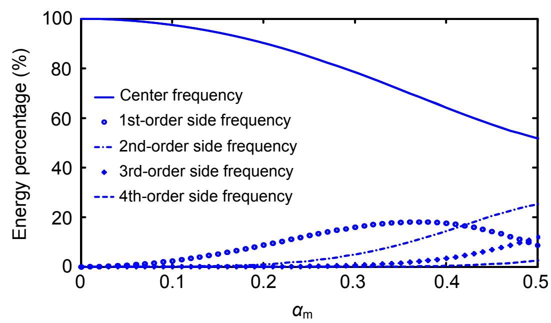

Fig. 13 Relationship between the energy percentage for each frequency component and α_m

is impossible and also unnecessary to obtain all the side frequency components. Thus, the weight of each frequency component is investigated to achieve a compromise in the design of BPF.

The variation of energy percentage for each frequency component with α_m is shown in Fig. 13. The energy percentage of the center frequency decreases rapidly with the increase of α_m, and even below 55% when α_m equals 0.5.

From an intuitive view, a calculation was made according to the mathematical model proposed in this study to compare the BPF among different pass bands.

Fig. 14 shows that more than 97.5% of the energy is included when the pass band is larger than $[\omega_s-3\omega_c, \omega_s+3\omega_c]$.

We can make the following comments on the basic design principle of the BPF:

1. Smooth pass band gain (for example, Butterworth filter) is recommended to let all the frequency components pass through with the same gain; this is the basic requirement to reconstruct A_1 in the time domain according to the Parseval theorem.

2. A narrow band filter is not suitable, because the bandwidth should be large enough to include at least the 3rd-order side frequency component.

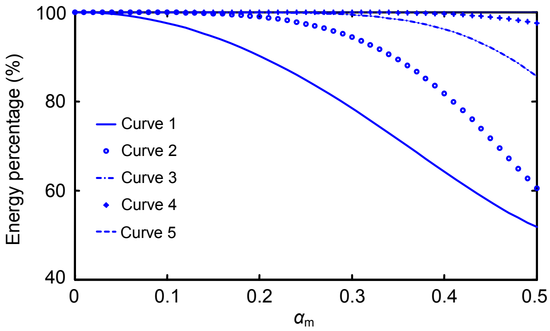

Fig. 14 A contrast of band-pass filters (BPFs) with different bandwidths

Curve 1 describes an ideal BPF that can extract only the center frequency; curve i (i=2, 3, 4, 5) describes an ideal BPF with the pass band that can extract not only the center frequency, but also the (i−1)th-order side frequency component included

3. Excessive bandwidth cannot further increase the signal-to-noise ratio (SNR) because the amplitude of the high-order side frequency component is equal to the amplitude of the noise. According to Eq. (13), the designed bandwidth should not be too wide to include the higher harmonics of the current ripple.

From these basic principles, the bandwidth of the BPF has a sufficient margin; one can seek an optimal design for the maximum SNR within this margin. However, practical experience shows that it makes no obvious difference as long as the BPF satisfies these basic principles.

According to the parameters of the platform used in this study, the pass band of BPF is designed as [5, 35] kHz. A Butterworth filter is used. The BPF is realized by cascading an LPF and an HPF using the chip UAF42. The designed transfer function is

$$H_{\mathrm{BPF}}=\frac{as^2}{s^4+bs^3+cs^2+ds+h}, \tag{25}$$

where a=4.84×10^{10}, b=3.55×10^{5}, c=6.32×10^{10}, d=2.46×10^{15}, h=4.77×10^{19}.

Fig. 15 shows the hardware photograph of the BPF board.

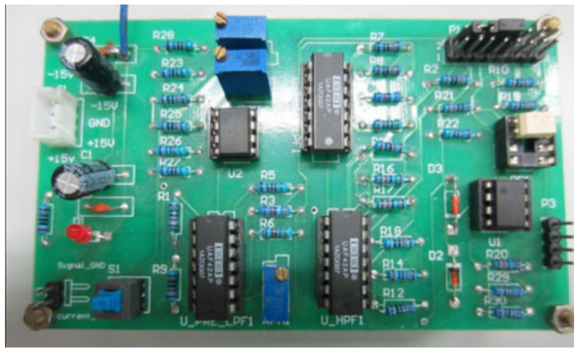

Fig. 15 Band-pass filter (BPF) board using UAF42

7 Suspension experiments

7.1 Static examination

In this examination, the AMB system is suspended with a position sensor as its feedback; the estimator is used only to compare with the output of the position sensor. The rotor can be suspended at a different position by changing the reference position. Then the outputs of the position sensor and the estimator are collected at the same time for examining the linearity and accuracy of the estimator (Fig. 16). Note that:

1. To avoid magnetic saturation, the bias current is set to about 0.5 A for each coil.

2. The geometric center of the stator is selected as the zero position of each direction. So, the range of each direction is [−250, 250] μm.

3. The output voltages of the position sensor and the estimator are both mapped to [0, 3] V to meet the input voltage level of DSP.

X_L and Y_L are the rotor positions of the left AMB in the horizontal and vertical directions, respectively. X_R and Y_R are the rotor positions of the right AMB in the horizontal and vertical directions, respectively.

In Fig. 16, overall the estimator agrees with the sensor within the full scope, although not identical. The estimator of the right AMB has smaller variance than the left one. This is probably because the right AMB stays close to the motor, and thus the mechanical bearing of the motor may provide assistance in positioning. However, this hypothesis has not been experimentally proven.

7.2 Rotation experiment feedback by the estimator

In rotation experiments, the output of the estimator is used as the position feedback. Fig. 17 shows the rotor trajectory of the estimator at 1000 r/min. The output of the sensor is also recorded, for a comparison with the estimator (Fig. 18).

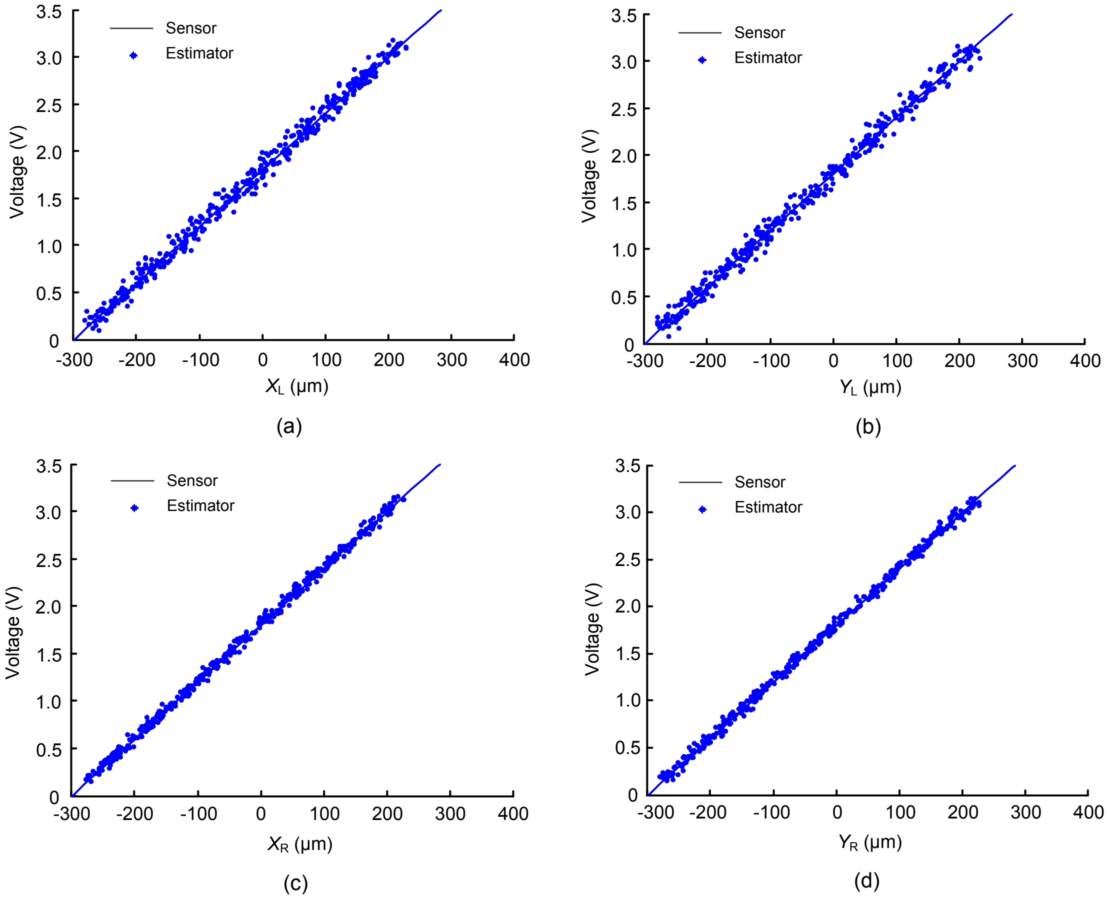

Fig. 16 Performance of the estimator in both active magnetic bearings (AMBs): (a) left AMB in the horizontal direction; (b) left AMB in the vertical direction; (c) right AMB in the horizontal direction; (d) right AMB in the vertical direction

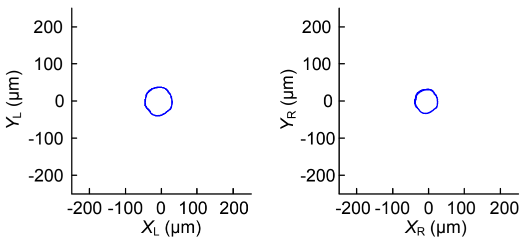

Fig. 17 Rotor trajectory of both active magnetic bearings (AMBs) at 1000 r/min

Because of the effect of the tangential electromagnetic force on the motor, the trajectory of the rotor seems a little messy during the acceleration process (from 1500 to 3000 r/min). Figs. 17–19 confirm the feasibility and excellence of the estimator. We can conclude that the position estimation using real-time duty cycle achieves satisfactory performance in the self-sensing AMB system.

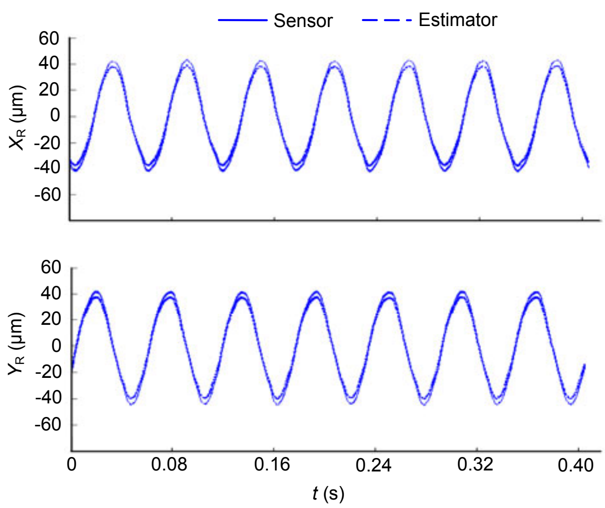

Fig. 18 Comparison between the sensor and the estimator of the right active magnetic bearing (AMB) at 1000 r/min

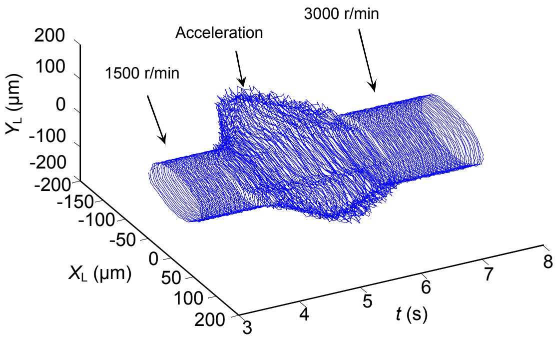

Fig. 19 Trajectory of the rotor which is accelerated from 1500 to 3000 r/min

8 Conclusions

A PWM power amplifier acts not only as the actuator, but also as a high frequency source. The frequency spectrum of this high frequency source has special characteristics that differ from conventional ones. The conventional high frequency source for inductance measurement always has a fixed frequency and tiny amplitude. However, the PWM has a complicated frequency spectrum.

Theoretical analysis shows that the time-varying duty cycle leads to the time-varying frequency spectrum of the coil current. The frequency spectrum of the current ripple at the switching frequency includes a center frequency and infinite side frequency components whose amplitudes are given by the Bessel function, and the frequency interval between each side frequency equals the frequency of the reference current.

Experimental results confirmed the theoretical analysis that the peaks not only occur at the right frequencies, but have the right amplitudes with a very small error caused by unavoidable noise. The detailed analysis of the current ripple in the frequency domain provides a solid theoretical foundation to the design principle of the BPF in the signal extraction strategy.

A strategy for position estimation is proposed using real-time duty cycle. The accuracy and linearity of this estimator are tested and verified in a static state. The rotation experiment shows that the strategy proposed is feasible and that the performance of this kind of estimator is satisfactory for self-sensing AMBs.

References

Garcia, P., Guerrero, J.M., Briz, F., Reigosa, D.D., 2010. Sensorless control of three-pole active magnetic bearings using saliency-tracking-based methods. *IEEE Trans. Ind. Appl.*, **46**(4):1476-1484. [doi:10.1109/TIA.2010.2049973]

Li, L.C., Shinshi, T., Shimokohbe, A., 2004. State feedback control for active magnetic bearings based on current change rate alone. *IEEE Trans. Magn.*, **40**(6):3512-3517. [doi:10.1109/TMAG.2004.836295]

Maslen, E.H., 2006. Self-Sensing for Active Magnetic Bearings: Overview and Status. Proc. 10th Int. Symp. on Magnetic Bearings, p.13-19.

Maslen, E.H., Iwasaki, T., Mahmoodian, R., 2006. Formal Parameter Estimation for Self-Sensing. Proc. 10th Int. Symp. on Magnetic Bearings, p.206-210.

Montie, D.T., 2003. Performance Limitations and Self-Sensing Magnetic Bearings. PhD Thesis, University of Virginia, USA.

Noh, D., 1997. Self-Sensing Magnetic Bearings Driven by a Switching Power Amplifier. PhD Thesis, University of Virginia, USA.

Okada, Y., Matsuda, K., Nagai, B., 1992. Sensorless Magnetic Levitation Control by Measuring the PWM Carrier Frequency Component. Proc. 3rd Int. Symp. on Magnetic Bearings, p.176-183.

Ranft, E.O., van Schoor, G., du Rand, C.P., 2011a. Self-sensing for electromagnetic actuators. Part I: a coupled reluctance network model approach. *Sens. Actuat. A*, **172**(2):400-409. [doi:10.1016/j.sna.2011.09.041]

Ranft, E.O., van Schoor, G., du Rand, C.P., 2011b. Self-sensing for electromagnetic actuators. Part II: position estimation. *Sens. Actuat. A*, **172**(2):410-419. [doi:10.1016/j.sna.2011.09.037]

Schammass, A., Bleuler, H., 2002. Experimental Result on Self-Sensing AMB Using a Three-State PWM Amplifier. Proc. 8th Int. Symp. on Magnetic Bearings, p.289-292.

Schammass, A., Herzog, R., Buhler, P., Bleuler, H., 2005. New results for self-sensing active magnetic bearings using modulation approach. *IEEE Trans. Control Syst. Technol.*, **13**(4):509-516. [doi:10.1109/TCST.2004.843142]

Sivadasan, K.K., 1996. Analysis of self-sensing active magnetic bearings working on inductance measurement principle. *IEEE Trans. Magn.*, **32**(2):329-334. [doi:10.1109/20.486516]

Tang, M., Zhu, C.S., 2010. New Method of Position Estimation for Self-Sensing Active Magnetic Bearings Based on Artificial Neural Network. Int. Conf. on Electrical and Control Engineering, p.1355-1358. [doi:10.1109/iCECE.2010.336]

Vischer, D., 1988. Sensorlose und Spannungsgesteuerte Magnetlager. PhD Thesis, No. 8665, Department of Mechanical Engineering, Swiss Federal Institute of Technolology, Zurich, Switzerland.

Vischer, D., Bleuler, H., 1990. A New Approach to Sensorless and Voltage Controlled AMBs Based on Network Theory Concepts. Proc. 2nd Int. Symp. on Magnetic Bearings, p.301-306.